

Enhancement of piezoelectric properties in a narrow cerium doping range of $\text{Ba}_{1-x}\text{Ca}_x\text{Ti}_{1-y}\text{Zr}_y\text{O}_3$ evidenced by combinatorial experiment

Kevin Nadaud,^{*,†} Guillaume F. Nataf,[†] Nazir Jaber,[†] Béatrice Negulescu,[†] Fabien Giovannelli,[†] Pascal Andrezza,[‡] Pierre Birnal,[‡] and Jérôme Wolfman[†]

[†]*GREMAN UMR 7347, Université de Tours, CNRS, INSA-CVL, 16 rue Pierre et Marie Curie, 37071 Tours, France*

[‡]*ICMN, CNRS, Université d'Orléans, 1b rue de la Férollerie, CS 40059, 45071 Orléans Cedex 02, France*

E-mail: kevin.nadaud@univ-tours.fr

Abstract

Lead-free materials based on the $(\text{Ba}, \text{Ca})(\text{Zr}, \text{Ti})\text{O}_3$ (BCZT) system exhibit excellent electromechanical properties that can be strongly modified by small amounts of dopants. Here, we use a combinatorial strategy to unravel the influence of aliovalent doping with Ce on dielectric and piezoelectric properties of BCTZ. We synthesize and characterize a single BCTZ thin film with a composition gradient from undoped to 0.2 mol% cerium doping. The cerium doping increases the piezoelectric coefficient from $42.3 \pm 2.9 \text{ pm V}^{-1}$ (undoped) to $63.0 \pm 2.4 \text{ pm V}^{-1}$ for 0.06 Ce-mol%, and then decreases to $38.4 \pm 1.3 \text{ pm V}^{-1}$ for the maximum amount of cerium (0.2 mol%). An investigation of sub-coercive field non-linearities reveal that these variations are not only induced by

changes in dynamics and densities of domain walls. The results highlight the advantage of combinatorial techniques to identify ideal compositions for applications, without synthesizing a high number of samples with unavoidable sample-to-sample variations.

Keywords

Combinatorial Pulsed Laser Deposition, Hyperbolic analysis, relaxor, domain wall, piezoelectricity, combinatorial experiment

1 Introduction

Thanks to their high dielectric permittivity and high piezoelectric coefficient, relaxor ferroelectrics are promising material for energy storage and actuators^{1,2}. In this context, BaTiO₃-based materials such as the Ba_{1-x}Ca_xTi_{1-y}Zr_yO₃ (BCTZ) solid solution represent an interesting alternative to lead-based materials³⁻⁶.

For BaTiO₃ derived materials, large piezoelectric coefficients have been found in the vicinity of the morphotropic phase boundary (MPB)⁷. It results from a complex interplay between chemistry, phase transitions and microstructures. For example, the dynamics of domain walls, in their ferroelectric phases, can enhance the electromechanical response⁸⁻¹⁰. In order to explore complex ternary diagrams using conventional synthesis, numerous samples are required, which can be challenging. Furthermore, unavoidable sample-to-sample variations introduce uncertainties into measured properties. In such context, combinatorial experiment emerged during the last decade to facilitate the exploration of phase diagrams by synthesizing samples with a continuous composition, structure or thickness variation¹¹. For the elaboration of samples with such gradients, combinatorial pulsed laser deposition (CPLD) can be used^{4,12-14}. In addition to the application motivation, i.e. finding the optimum composition to maximize a given property, the combinatorial techniques permit to continuously explore phase diagrams and allows a fine determination of phase transitions.

In this article, we use the combinatorial experiment to investigate the effect of cerium doping on dielectric and piezoelectric properties of $0.5(\text{Ba}_{0.7}\text{Ca}_{0.3}\text{TiO}_3) - 0.5(\text{BaZr}_{0.2}\text{Ti}_{0.8}\text{O}_3)$ thin films. We chose to work with cerium since there exist already some reports on the influence of cerium doping on the dielectric and piezoelectric properties of BCTZ ceramics, revealing enhanced properties in a narrow composition range (0.025 to 0.25 mol% of Ce)¹⁵ with few (3) tested compositions. The literature also contains contradictory results, e.g. on the evolution of phase transition temperatures with different Ce content¹⁶⁻¹⁹. Furthermore, the influence of Ce-doping on a BCTZ thin film has not been investigated so far.

Two samples were realized: an undoped BCTZ sample to calibrate the sensitivity of the piezoelectric characterization tool and to verify the homogeneity of the deposition technique and a second sample with a composition gradient from undoped to 0.2 mol% cerium doping. In addition to conventional dielectric spectroscopy, sub-coercive field non-linearities have been studied using modified Rayleigh analysis and discussed in terms of modification of dielectric and piezoelectric properties.

2 Experiments

Polycrystalline BCTZ film were deposited on Pt/TiO₂/MgO substrates (10 mm × 10 mm, (001) oriented) by combinatorial pulsed laser deposition (CPLD) technique^{4,12} in a vacuum chamber with a base pressure of 5×10^{-8} mbar. A MgO substrate was preferred to Si to minimize thermal stress during the cooling process. A homogenized excimer laser beam (KrF, $\lambda = 248$ nm, 12 ns–20 ns) pass through a square aperture whose focused image is swept over the surface of a homemade Ba_{0.85}Ca_{0.15}Ti_{0.9}Zr_{0.1}O₃ ceramic target (BCTZ₅₀) or a homemade 0.2% Ce-doped Ba_{0.85}Ca_{0.148}Ce_{0.002}Ti_{0.9}Zr_{0.1}O₃ ceramic target (Ce₀₂:BCTZ₅₀). The resulting ablation plume scans over the entire substrate surface to ensure a good thickness and composition uniformity. Substrate temperature, oxygen pressure, laser fluence and repetition rate were optimized with respect to phase purity, crystallinity, surface roughness and

piezoelectric performances. During the growth of the films, the laser fluence was kept at 1.15 J cm^{-2} . The substrate temperature was held at 700°C with a dynamic O_2 pressure of 0.3 mbar . Cooling was realized under 500 mbar static oxygen pressure at 3°C min^{-1} cooling rate, with a 400°C dwell step of one hour to ensure good oxygenation of the film.

Two samples were synthesized. The first one is a reference sample deposited from a single undoped BCTZ target, (30000 laser pulses fired at 6 Hz). The second one was deposited by combinatorial PLD using the undoped BCTZ target and a Ce-doped BCTZ target ($0.2\% \text{ mol}$). The combinatorial approach takes advantage of the very directional PLD plume to localize the deposition at the surface of the substrate using a mask with a rectangular aperture (shadow masking). Sliding this aperture, close to the substrate, in one direction combined with a small deposition rate ($39 \text{ pulses / perovskite unit cells uc}$ with the mask) allow “distributing” the deposited material on the surface. By synchronizing the mask movements with the laser pulses fired on the undoped target, a controlled wedge of BCTZ is fabricated in a first deposition step: one side of the substrate “sees” 156 laser pulses, corresponding to 4 unit cells (uc), while on the opposite substrate side there is no deposition (see schematic Fig. 1a). Next, the complementary sequence of mask positioning and laser firing on the doped target is realized to complete the 4 uc thickness on the substrate surface with Ce-doped BCTZ. This two-steps deposition sequence is repeated 250 times, targeting a final thickness of about 400 nm (1000 uc). The resulting film has a composition that varies from BCTZ_{50} to $\text{Ce}_{0.2}:\text{BCTZ}_{50}$ in the x direction, while it is kept constant in the y direction (Fig. 1a). Mask-substrate relative positioning at deposition temperature has an accuracy of a few hundreds of microns, leading to an offset of the composition gradient versus nominal position. To localize the experimental gradient and access its total nominal extent, 1 mm wide bands with constant composition are framing the composition gradient in the sample design (Fig. 1c).

Top Au electrodes (diameter $330 \mu\text{m}$) were then sputtered through a shadow mask. An array of 91 capacitors is thus defined with 13 columns along the gradient direction and 7

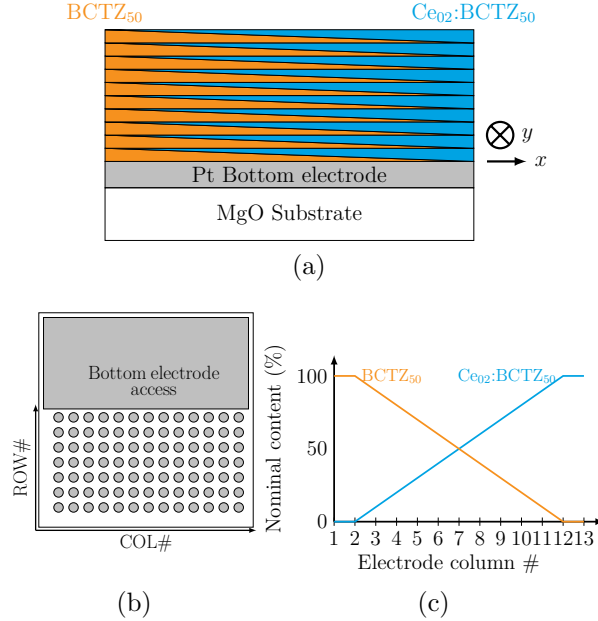


Figure 1: Side view schematic of the sample with a doping gradient (a). Schematic of the sample with row/column convention (b). Nominal gradient for the Ce_x :BCTZ sample (c).

lines for repetitions (Fig. 1b) for the Ce_x :BCTZ₅₀ doped sample. With the lateral constant composition bands, 11 different compositions are accessible (columns 2 to 12). The same mask design was used for the undoped BCTZ₅₀ sample, leading to the definition of 91 capacitors with the same nominal composition to characterize the deposition homogeneity.

Phase analysis and local structural investigations were conducted using X-ray micro-diffraction (parallel beam of Cu K_α mean radiation, Bruker Discover). Absolute global chemical composition and thickness were determined by Rutherford Back Scattering (RBS) on homogeneous BCTZ₅₀ sample while local composition/thickness variations of both Ce_x :BCTZ₅₀ and BCTZ₅₀ were characterized by Wavelength Dispersive Spectroscopy (WDS). Conventional WDS (or EDS) model assume a homogeneous sample at the electron probe level. The layered nature of our samples imposed to acquire emitted photons at various e-beam acceleration voltages. The voltage dependency of the intensity ratio coming from sample and standards (a.k.a. K -ratio) were then simulated by STRATAGEM software in order to extract thickness/composition variations for Ba, Ca, Ti and Zr (exemple shown Fig. S3). The small Ce doping level (up to 0.2 mol%) prevented Ce detection using WDS. Surface

sensitive X-ray Photoelectron Spectroscopy (XPS) has been attempted to evidence the Ce doping gradient.

The dielectric characterizations presented in this article have been acquired using a lock-in amplifier (MFLI with MD option, Zurich Instrument) connected to a temperature-controlled probe station, having a motorized chuck (Summit 12000, Cascade Microtech). The AC measuring signal has been generated using the embedded lock-in generator. Its amplitude has been swept from 10 mV_{rms} to 1 V_{rms} at a frequency of 10 kHz. The applied voltage and current through the capacitor are measured simultaneously by the lock-in and are demodulated simultaneously. $|V| \exp(j\theta_V)$ is the phasor representing the applied voltage and $|I| \exp(j\theta_I)$ the phasor representing the current (with j the imaginary unit). The first harmonic of the current and the applied voltage are used to compute the complex impedance:²⁰⁻²³

$$Z = \frac{|V|}{|I|} \exp(j(\theta_V - \theta_I)) \quad (1)$$

The complex capacitance C^* can hence be derived from the complex impedance:

$$C^* = \frac{1}{j\omega Z} = \frac{|I|}{\omega|V|} \exp\left(j\left(\theta_I - \theta_V - \frac{\pi}{2}\right)\right) \quad (2)$$

with ω the angular frequency of the measuring voltage. The material relative permittivity ϵ_r^* is:

$$\epsilon_r^* = \frac{t}{S\epsilon_0} C^*, \quad (3)$$

with t the thickness of the film, S the surface of the electrodes and ϵ_0 the vacuum permittivity. In the present case, the electrodes are sufficiently thick to limit the effect of the series resistance on the measured impedance.

For the phase transition temperature determination T_{max} , an AC measuring voltage of 10 mV_{rms} has been preferred in order to avoid underestimations due to domain wall motion contribution²³. T_{max} have been determined from the least square fitting of ϵ_r' with a

parabola^{23,24}.

The ferroelectric and piezoelectric characterizations have been performed with an Aix-ACCT DBLI and TF2000 ferroelectric analyzer (aixACCT Systems GmbH, Germany) using a triangular waveform at a frequency of 1 kHz and a magnitude of 5 V. An automated chuck allows measuring the properties as function of the position of the electrode. To ensure a good reflection of the laser beam, aluminum has been deposited on the back side of the sample. The current is measured using the virtual ground method and the polarization is computed using numerical integration with respect to the time. To improve the signal to noise ratio, the results of $P(E)$ and $S(E)$ loops correspond to the average over 1000 periods. The calculation of the piezoelectric coefficients has been made using a linear regression from the maximum, respectively minimum field value to 0 kV cm^{-1} for positive, respectively negative, fields. The linear regression has two advantages (i) it is less sensitive to noise and (ii) it provides a confidence indicator on the extracted value, coming from the regression algorithm.²⁰ The presented piezoelectric coefficient is the average value between the piezoelectric coefficient for positive and for negative field. To investigate the asymmetry of the $S(E)$ loop, the difference between positive and negative fields piezoelectric coefficient is also computed and noted Δd_{33}^* .

3 Result and discussion

The properties of undoped BCTZ sample are initially presented, focusing homogeneity of thickness, composition, dielectric and piezoelectric properties, as described in the first section of the article. Then, the dielectric and piezoelectric properties of the Ce-doped BCTZ sample ($\text{Ce}_x\text{:BCTZ}_{50}$) are presented and compared to the reference properties measured on the BCTZ_{50} sample. In the third section, the effect of cerium doping on domain wall motion contribution is investigated.

3.1 Undoped BCTZ

X-ray diffraction pattern shows that the BCTZ₅₀ film is single-phase to the detection limit and poly-oriented (see Fig. S1 in supplementary information of ref²³). Peak positions could be indexed according to orthorhombic BCTZ₅₀ (icdd pdf #04-022-8189). However the weak diffraction intensity from the poly-oriented film prevents to conclude on the exact symmetry (orthorhombic, rhombohedral, tetragonal,...). A diffraction pattern acquired at higher angle ($82.8^\circ < 2\theta < 84.6^\circ$) (see Fig. S1 in supplementary material) exhibits an asymmetric peak with at least three contributions. This implies the presence of more than one symmetry as it is to be expected close to a MPB. The BCTZ₅₀ film composition from RBS characterization (see Fig. S2a,b ref²³) was found to be close to the nominal target composition determined by WDS (see table S1 in supplementary material).

The local composition of the BCTZ₅₀ sample has been studied using WDS (e-beam footprint of 10 μm) and the results are reported as a function of the position on the sample (see Fig. S3 and S4 in supplementary material). For all elements, the ratio between 3σ dispersion and the mean value is below 3 %.

The thickness has been extracted as a function of the position using WDS (see Fig. S4 in supplementary material). An average thickness of 370 nm is obtained for the undoped sample, neglecting its outskirts. When considering the whole sample, the ratio between 3σ dispersion and the mean value is 10 % but it decreases to 7 % when discarding edges of the sample. All these data confirm the high uniformity of the composition and thickness of the BCTZ₅₀ sample.

Fig. 2a shows the dielectric permittivity as a function of temperature, for various representative electrodes on the sample. The temperature evolution follows the same trend for all electrodes, with a maximum at $330.2 \pm 1.3\text{ K}$, which is attributed to the ferroelectric to paraelectric phase transition²³. This value is closed to what has been found for BCTZ thin films in literature (323 K)^{25,26}. The transition temperature is highly homogeneous for all electrodes on the sample (Fig. 2b) since a standard deviation of 1.3 K is obtained. A

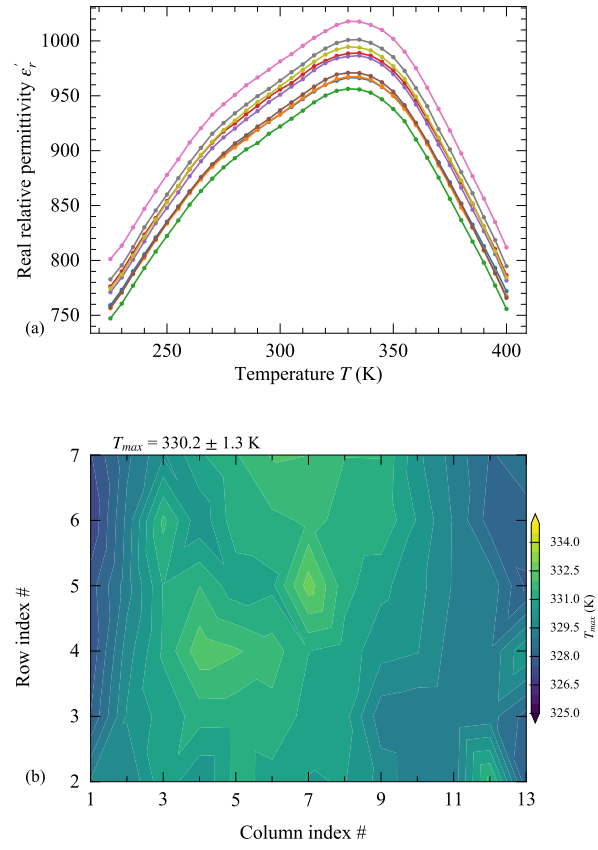


Figure 2: Relative permittivity as function of temperature for some selected capacitors (a) and T_{max} map (b) for undoped BCTZ₅₀ sample.

ferroelectric-ferroelectric transition is visible around 270 K which may correspond to T-O transition observed in bulk BCTZ₅₀.

Fig. 3a,b show the polarization and the strain for several electrodes on the sample. The $P(E)$ loop is typical of relaxor ferroelectrics with a small remnant polarization and a slim shape. Using the $P(E)$ loop, maximum and remnant polarizations have been computed for all capacitors and reported in Fig. 3c. Average values of $\Delta P_m = 21.1 \pm 1.1 \mu\text{C cm}^{-2}$ and $\Delta P_r = 3.4 \pm 0.2 \mu\text{C cm}^{-2}$ are obtained for the sample.

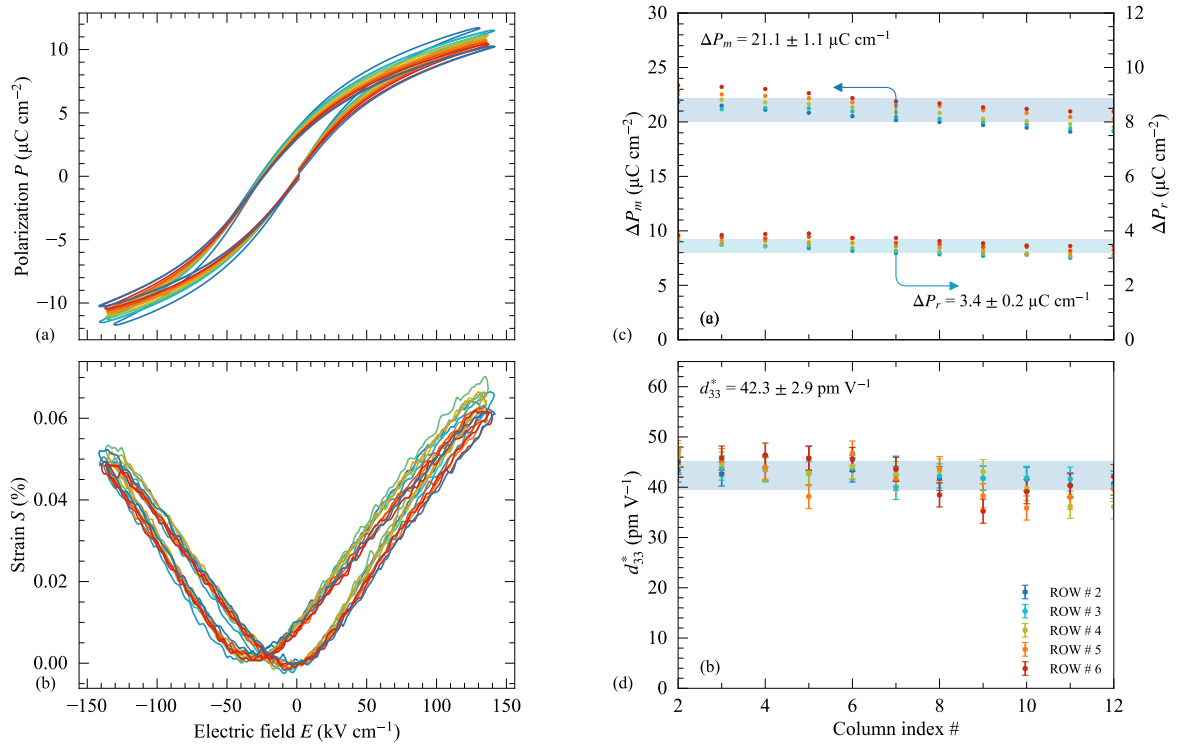


Figure 3: Polarization (a) and strain (b) as a function of the applied electric field for various electrodes on the BCTZ₅₀ sample. Maximum polarization and remnant polarization (c) and piezoelectric coefficient (d) for the BCTZ₅₀ sample. The shaded area represents the mean value and the standard deviation interval. The error bar for the d_{33}^* data points corresponds to the measurement resolution, estimated from 10 successive measurements of a single capacitor.

The horizontal shift of $P(E)$ and $S(E)$ loops is well visible since coercive field values are $E_c^+ = 2.5 \pm 0.9 \text{ kV cm}^{-1}$ and $E_c^- = -33.1 \pm 1.6 \text{ kV cm}^{-1}$. This shift reveals the presence of an internal bias field, which can result from Schottky barriers at the electrodes and/or internal

defects and polar nanoregions (PNRs)²³.

Fig. 3c,d presents the maximum polarization, the remnant polarization and the piezoelectric coefficient as a function of the position on the sample. The average value of the piezoelectric coefficient is $42.3 \pm 2.9 \text{ pm V}^{-1}$. The DBLI resolution for piezoelectric coefficient determination was estimated from 10 successive measurements of a single capacitor, leading to a dispersion of 2.4 pm V^{-1} (1σ). This compares with the dispersion found across the sample (2.9 pm V^{-1}).

All the results presented in this first part show the high uniformity of the composition and the dielectric/piezoelectric properties on a homogeneous BCTZ₅₀ sample and establish an upper limit for the resolution in d_{33}^* characterization.

3.2 Ce-doped BCTZ

The composition of the Ce_x:BCTZ₅₀ sample has been measured using the same procedure as described previously and the results are given in supplementary material (Fig. S5). The uniformity concerning Ba, Ca, Ti and Zr species is similar to the BCTZ₅₀ reference sample. Given the very small amount of Ce used, (maximum Ce molar concentration of 0.2%), WDS could not be used to confirm the effective concentrations. XPS Ce 3d spectrum have been acquired along the nominal gradient and are presented in Fig. S6. An evolution of Ce 3d signal is evidenced along the gradient as expected. However quantification from the weak Ce 3d signal is not possible. One can note a very weak but non-zero signal at the nominally undoped position. An average thickness of 476 nm is obtained from WDS for the doped sample not considering its outskirts.

Fig. 4 shows the effect of the Ce on the dielectric permittivity on some representative capacitors. When the Ce content increases, T_{max} decreases from 320 K to 260 K and the maximum permittivity value goes from 1050 to 810. Thus, at ambient temperature, for undoped and low Ce-content (columns 1/2) the material is into the ferroelectric phase. For a Ce-content estimated to 0.02% (columns 3/4), the material is in the transition region

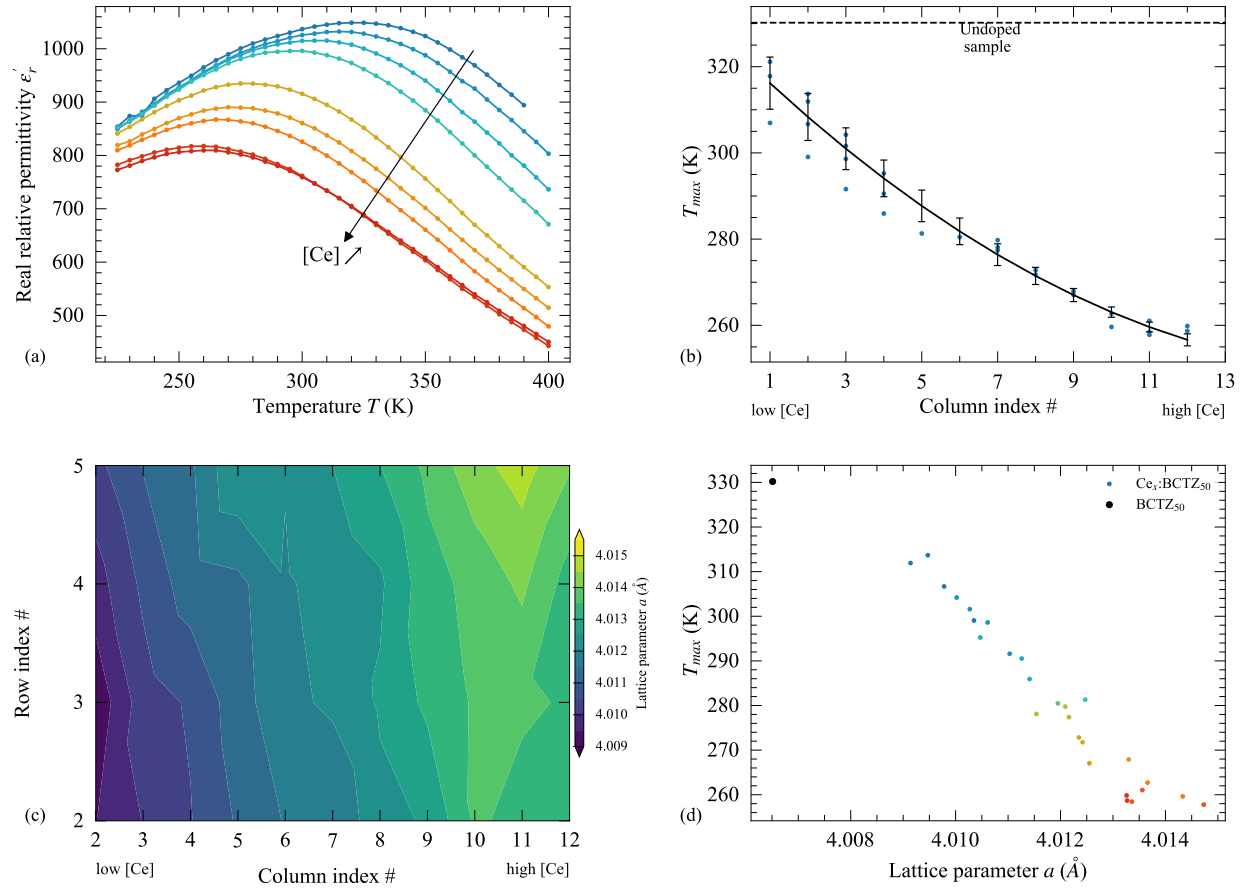


Figure 4: Relative dielectric permittivity as a function of temperature for some selected capacitors having different column number (a). T_{max} as a function of the column number (b). Lattice parameter computed using the interplanar spacing as a function of position on the sample (c). T_{max} as a function of the d_{204} (orthorhombic) or d_{222} (tetragonal or cubic) lattice parameter (d).

between ferroelectric and paraelectric. For larger Ce-content (above column 5), the material is in the paraelectric phase. The decrease of T_{max} suggests the Ce substitutes the A site element (Ba or Ca here) since for B site substitution, no change of the phase transition temperature is visible in BaTiO₃²⁷. Nevertheless, the change in T_{max} in our case is 15 times larger $-70\text{ K}/0.2\text{ mol}\%$ vs $-4.5\text{ K}/0.2\text{ mol}\%$ in²⁷.

Room temperature (RT) X-ray $\theta-2\theta$ micro-diffraction (500 μm collimator) patterns were acquired for capacitors from column 2 to 12 for lines 2 to 5 (44 patterns) around $2\theta = 83.5^\circ$. The beam footprint on the sample in the gradient direction is 500 μm and perpendicular to this direction 670 μm ($\simeq \frac{500}{\cos\theta}$). All these patterns exhibit a single peak (see Fig. S2 in supplementary material) which could be indexed $(222)_{C,T}$, $(204)_O$ or $(240)_O$, $(006)_R$ or $(042)_R$ depending on the actual symmetry (respectively cubic, tetragonal, orthorhombic, rhombohedral). When T_{max} is below RT (columns 5-12) the RT symmetry is cubic (paraelectric phase) while for $T_{max} > \text{RT}$ we cannot conclude on the symmetry. The FWHM of the observed diffraction peaks is independent of Ce content. The interreticular distance was extracted versus sample position using Bragg relation. The corresponding pseudo-cubic lattice parameter is represented as a map in Fig. 4c. A predominantly horizontal gradient of the lattice parameter is observed and correlates to the nominal Ce gradient: the lattice parameter progressively increases when the Ce content increases, confirming that Ce is entering into the perovskite phase. Taking a closer look to Fig. 4c one can see that the lines are not strictly vertical, indicating a slight variation of the lattice parameter, and hence of the Ce content, along columns with nominal constant composition. In fact there is a quasi-continuum of lattice parameter (and hence of Ce doping) across the sample correlated to a quasi-continuum of T_{max} as can be seen of Fig. 4d.

The highest observed T_{max} for the Ce_x:BCTZ sample ($\sim 322\text{ K}$ for column 1 line 2 see Fig. 4b) is lower than the value measured for the BCTZ₅₀ sample (330 K) while the smallest lattice parameter in the Ce_x:BCTZ (4.009 Å) is still higher than for BCTZ₅₀ undoped sample (4.006 Å) even for a zero Ce nominal content. This is attributed to the presence of a very

small amount of Ce even on the side expected to be undoped as can be seen from Ce 3d XPS signal (Fig. S6). This is confirmed by the fact that the data point of the undoped sample (in black) in Fig. 4d follows the trend but is far away from the rest of data points from Ce_x:BCTZ sample (colored)

The evolution of the phase transition temperature T_{max} is directly linked to the lattice parameter variation (Fig. 4d) as T_{max} regularly decreases when the lattice parameter increases corresponding to the increase of Ce content. As a direct measurement of Ce content is not experimentally accessible given its small content, we will use the lattice parameter as an indirect indication of actual Ce content variation instead of the nominal Ce content in the following figures.

Figs. 5a and 5b show the polarization and the strain for several electrodes on the Ce_x:BCTZ₅₀ sample. When the Ce content increases, maximum polarization decreases and the $P(E)$ loop goes to a slimmer shape. An horizontal shift of the $P(E)$ and $S(E)$ loops is present, similar to what has been mentioned for the undoped sample. Fig. 5c shows the coercive and the internal field as a function of the lattice parameter. For low amount of Ce (lattice parameter between 4.009 Å and 4.0106 Å), the lower coercive field E_c^- is similar to undoped BCTZ whereas the upper coercive field E_c^+ is more negative (-12 kV cm^{-1} vs 2.5 kV cm^{-1}), resulting in a larger internal bias field (-24 kV cm^{-1} vs -16 kV cm^{-1}). When the Ce content increases, the difference between coercive field decreases, corresponding to the slimmer shape described previously, and the internal bias field slightly decreases (in absolute value) from -24 kV cm^{-1} to -20 kV cm^{-1} . This evolution of the internal bias may reveal an evolution of the PNR density with the amount of Ce²³.

Fig. 6 shows the ferroelectric and piezoelectric properties for the Ce_x:BCTZ₅₀ sample. When Ce content increases, maximum polarization decreases from $\Delta P_m = 21.1 \pm 1.1 \mu\text{C cm}^{-2}$ to $\Delta P_m = 13.4 \pm 0.3 \mu\text{C cm}^{-2}$ and the remnant polarization decreases from $\Delta P_r = 3.4 \pm 0.2 \mu\text{C cm}^{-2}$ to $\Delta P_r = 0.80 \pm 0.03 \mu\text{C cm}^{-2}$. This large decrease of the polarization has been observed for BCTZ ceramics only for Ce content above 0.25 %¹⁵. For this reason, the

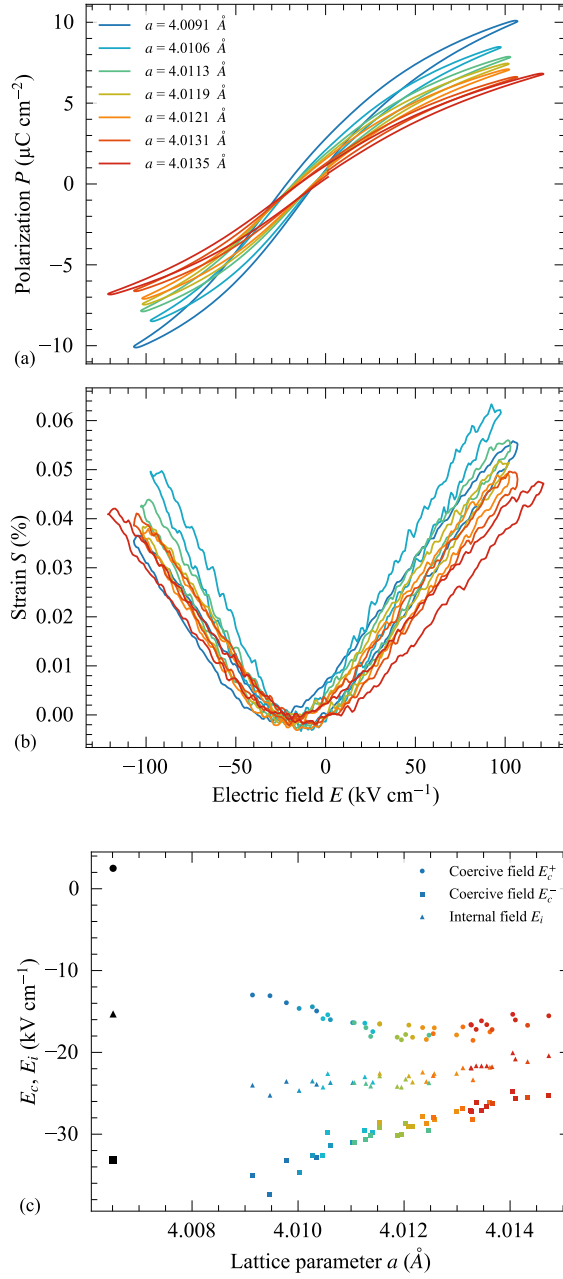


Figure 5: Polarization (a) and strain (b) as a function of the applied electric field for different compositions (having a different lattice parameter) present on the $\text{Ce}_x\text{:BCTZ}_{50}$ sample. Coercive and internal field as a function of the lattice parameter (c). Black symbols correspond to the undoped sample.

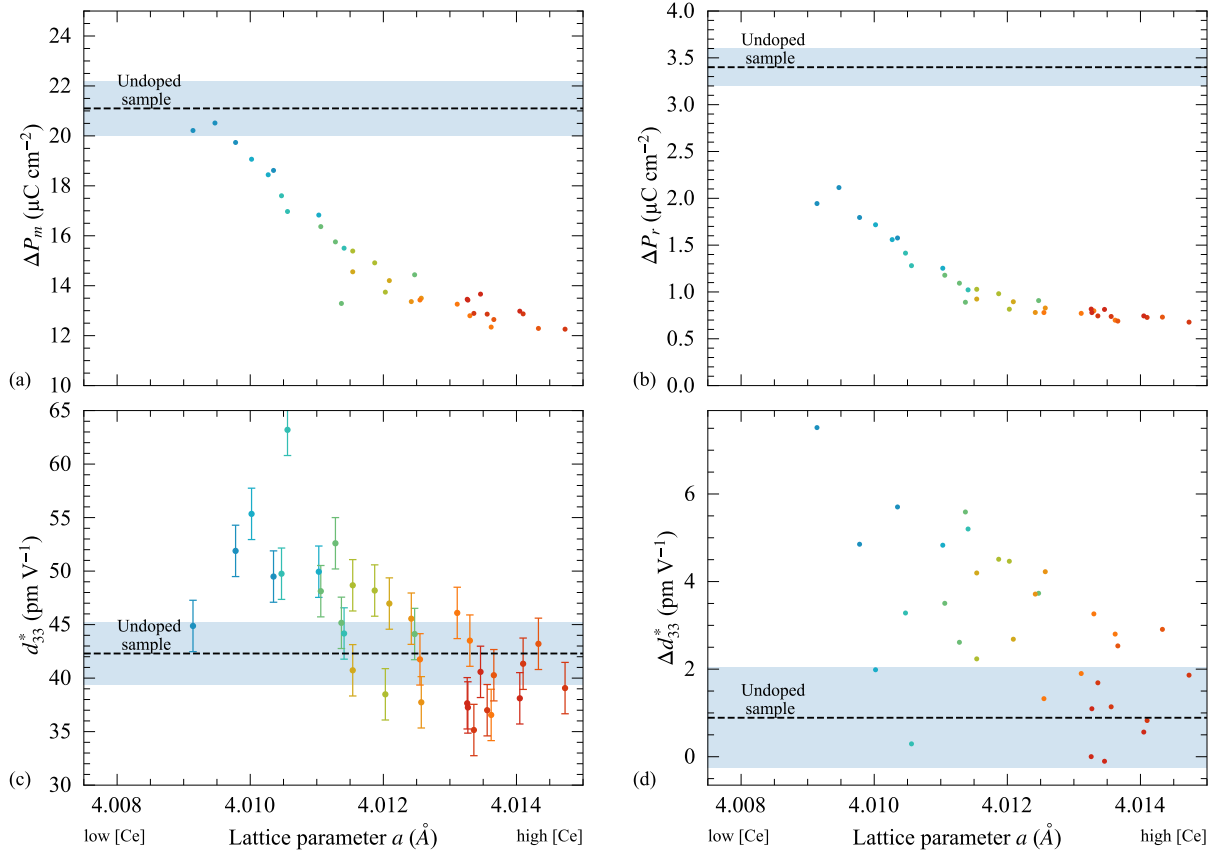


Figure 6: Maximum polarization (a), remnant polarization (b), piezoelectric coefficient (c) and difference between positive and negative branch piezoelectric coefficient (d) for the $\text{Ce}_x\text{:BCTZ}_{50}$ sample, as a function of the lattice parameter.

decrease of maximum and remnant polarizations is attributed here to the decrease of the phase transition temperature T_{max} when the Ce content increases: for composition having a lattice parameter above 4.0105 Å, ambient temperature is above T_{max} and thus supposed to be in the paraelectric phase.

The piezoelectric coefficient sharply increases by 50 % from $42.3 \pm 2.9 \text{ pm V}^{-1}$ (for the undoped sample) to $63.0 \pm 2.4 \text{ pm V}^{-1}$ for a Ce-content estimated to about 0.06 % (lattice parameter of 4.0105 Å), then sharply decreases back to about 42 pm V^{-1} for a Ce-content estimated to 0.11 % (lattice parameter of 4.0125 Å). After that, a slow decrease of d_{33}^* up to the maximum amount of cerium (0.2 %, lattice parameter of 4.0147 Å).

The sharp d_{33}^* peak could be evidenced solely because sub-nominal 0.02 % steps variations of Ce content were obtained in this quasi-continuous gradient sample. The very small amount of cerium needed to enhance the piezoelectric properties is close to what was found in ceramics¹⁵. Indeed Hayati and co-workers showed that 0.05 % of Ce doping was better than 0.025 % and 0.25 %. However with such big steps they may have missed the optimum doping. This result strengthen the interest of the combinatorial approach and call for denser capacitors array associated with less steep gradient and thorough x-ray micro-diffraction analysis.

The difference between positive and negative fields piezoelectric coefficient Δd_{33}^* is reported Fig. 6d. A small amount of Ce (lattice parameter between 4.009 Å and 4.0105 Å) largely increases Δd_{33}^* compared to the undoped sample, and when the amount of Ce increases, Δd_{33}^* progressively decreases. This evolution may be related to the evolution of the internal field (Fig. 5c).

3.3 Domain wall motion contribution

To determine if the change in piezoelectric properties is intrinsic or extrinsic, the evolution of ferroelectric domain walls and their motions have been investigated by measuring the relative permittivity as a function of the AC field. Due to the presence of irreversible domain

wall motion contribution (also called pinning/unpinning), the relative permittivity increases when the AC measuring field increases²⁸. In the case of homogeneous distribution of pinning centers, the relative permittivity linearly increases:

$$\varepsilon_r = \varepsilon_{r-l} + \alpha_r E_{AC} \quad (4)$$

ε_{r-l} correspond to the low field permittivity and α_r to the slope and represents the irreversible domain wall motion contribution.

In real materials, the distribution of pinning centers is not homogeneous and the linear increase is only visible after a given threshold²⁹⁻³¹. For low field, domain walls can only vibrate around an equilibrium position and the contribution is called reversible. In that case, the relative permittivity evolution with the measuring field can be described using the hyperbolic law:^{23,32,33}

$$\varepsilon_r = \varepsilon_{r-l} + \sqrt{\varepsilon_{r-rev}^2 + (\alpha_r E_{AC})^2} \quad (5)$$

with ε_{r-rev} the reversible domain wall motion contribution, proportional to the domain wall density³⁴⁻³⁶.

Fig. 7a shows the relative permittivity variation (difference in relative permittivity with respect to the value for $V_{AC} = 0.014$ V) as a function of the AC measuring field. When cerium content increases, the relative permittivity variations decrease, which corresponds to a lower irreversible domain wall motion contribution. By fitting the relative permittivity as a function of the AC measuring field using (5), it is possible to extract the reversible and irreversible domain wall motion contribution for different compositions and for different temperatures.

Fig. 7b,c shows the reversible and irreversible domain wall motion contributions as function of the lattice parameter for $T = 295$ K. At room temperature (295 K), both reversible and irreversible domain wall motion contributions decrease when the Ce content increases and no sharp maximum is visible for a lattice parameter of 4.0105 Å, the electrode where the

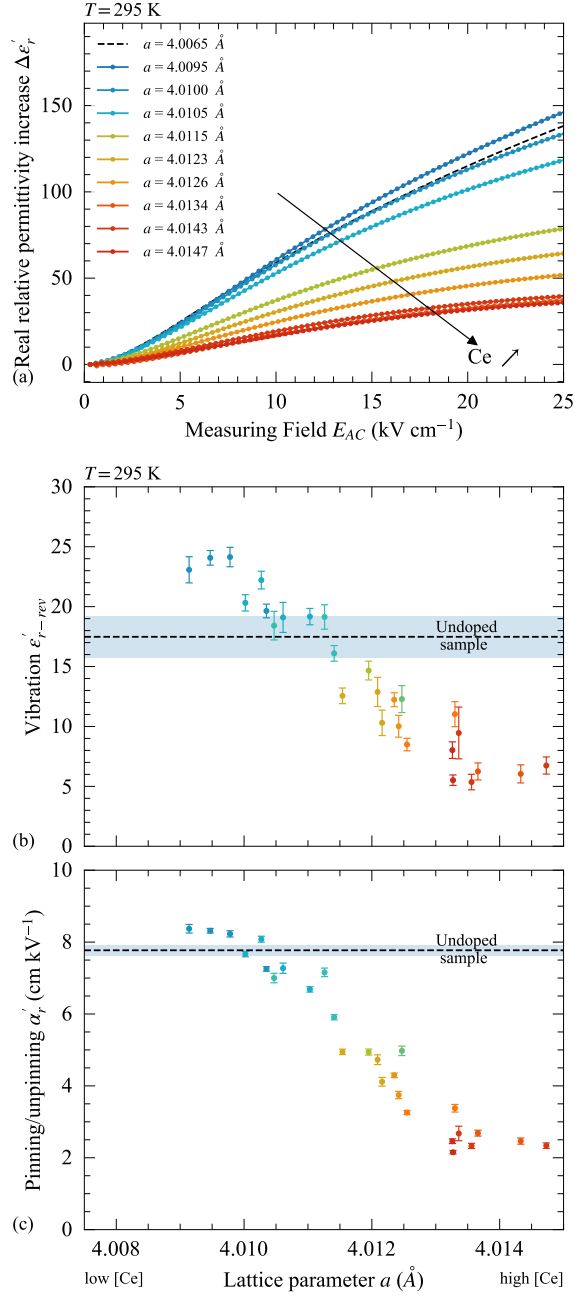


Figure 7: Relative permittivity variation as a function of the AC measuring field for $T = 295$ K (a). Reversible (b) and irreversible (c) domain wall motion contributions to the permittivity as a function of the lattice parameter at $T = 295$ K for the $\text{Ce}_x\text{:BCTZ}_{50}$ sample. Black dashed lines correspond to values extracted for the BCTZ_{50} with, the shaded area represents the mean value and the standard deviation interval.

piezoelectric coefficient is maximum. This indicates that the maximum value of the piezoelectric coefficient for this compound cannot be explained by a larger domain wall motion contribution (extrinsic). The irreversible contributions for low Ce content (lattice parameter lower than 4.011 Å) of the $Ce_x:BCTZ_{50}$ sample is very close to the ones obtained for the $BCTZ_{50}$ (black dashed line) and the reversible contribution is slightly higher.

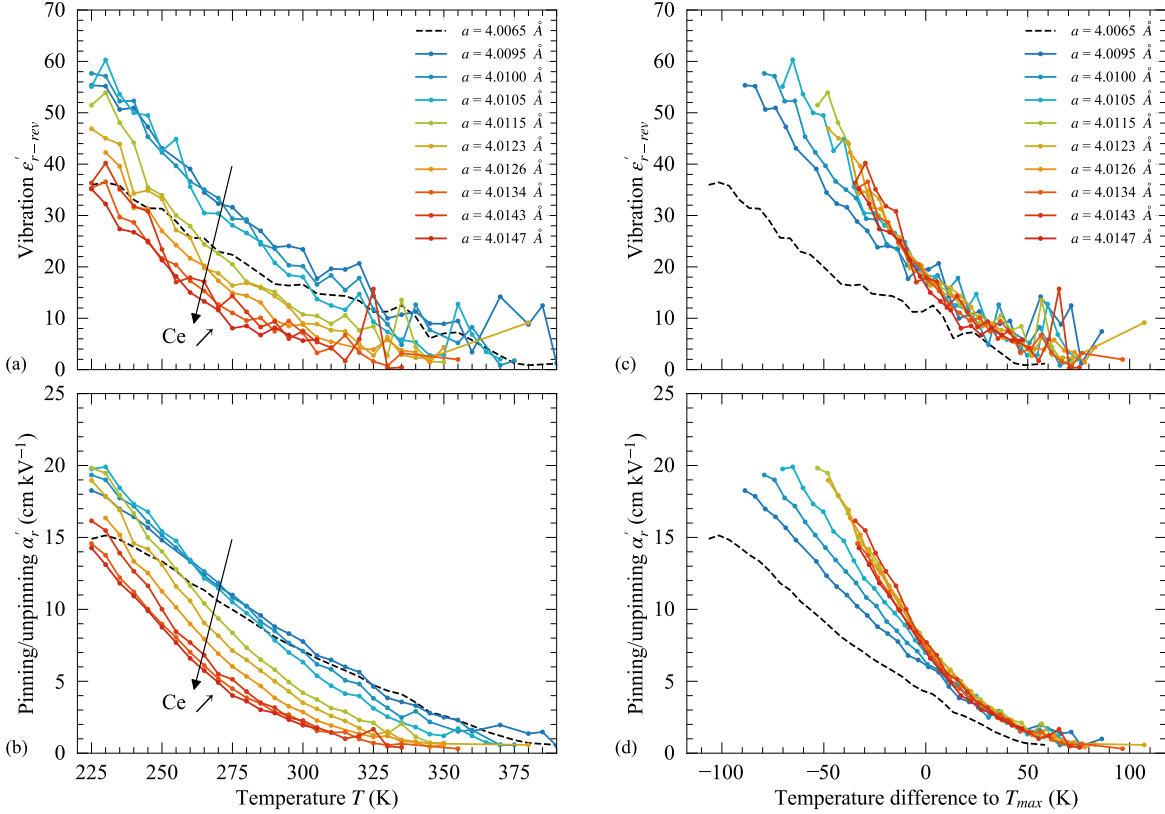


Figure 8: Reversible (a)-(c) and irreversible (b)-(d) domain wall motion contributions as a function of the absolute temperature (a)-(b) and the temperature relative to T_{max} (c)-(d), for different compositions (having a different lattice parameter) present on the $Ce_x:BCTZ_{50}$ sample. Black dashed lines correspond to values extracted for the $BCTZ_{50}$

Fig. 8a,b present reversible and irreversible domain wall motion contributions as a function of temperature for the different compositions of the $Ce_x:BCTZ_{50}$ sample. For all compositions, reversible and irreversible domain wall motion contributions decrease when temperature increases, which is also the case for pure $BCTZ$ ²³. This differs from what has been found for films of $(Pb, Sr)TiO_3$ ³³ or $0.5 PbYb_{1/2}Nb_{1/2}-0.5 PbTiO_3$ ³⁷ for which the domain

wall motion contribution increases when the temperature approaches T_{max} . For low temperatures (below 250 K), the reversible and irreversible domain wall motion contributions increase (lattice parameter lower than 4.0105 Å), then both contributions decrease, when the cerium content increases.

To determine if the decrease of domain wall motion contributions is linked to the decrease of T_{max} , it is useful to plot the reversible and the irreversible domain wall motion contributions as a function of the temperature offset to T_{max} (Fig. 8c,d). Above T_{max} , the domain wall motion coefficients still decrease but are not null, corresponding to a residual ferroelectricity^{38,39}, which persists here 70 K above T_{max} . Above T_{max} , when rescaled with respect to the temperature difference to T_{max} , the decrease rate and the reversible and irreversible values are the same for all the compositions. For temperatures below T_{max} , reversible and irreversible domain wall motion contributions slightly increase (lattice parameter lower than 4.0115 Å), then stabilize, when the Ce content increases.

In ferroelectric materials, the density of domain walls depends on the distance with respect to the transition temperature⁴⁰. Here, if it were the only reason for variations in the number of domain walls, all the curves in Fig. 8c,d would overlap. The fact that it does not highlights that the energy landscape in the film depends also on local chemistry and strain changes induced by cerium-doping. While overall domain wall motion contributions decrease with increasing cerium-content (Fig. 8a,b), because of the decrease of the phase transition temperature T_{max} , at a given temperature difference to T_{max} a low amount of cerium is actually facilitating reversible and irreversible domain wall motions (Fig. 8c,d). This is also visible for $T = 225$ K, far below T_{max} (Fig. 8a,b), where a small amount of cerium increases domain wall motion contributions.

4 Conclusion

In this article, we use high-throughput experiment to investigate the cerium doping effect on the dielectric and piezoelectric properties of BCTZ₅₀ thin film deposited by pulsed laser deposition. The first part is dedicated to the measurement on a homogeneous sample. For all elements, the ratio between 3σ dispersion and the mean value is below 3% and for the thickness, the ratio is 10% (whole sample) but it decreases to 7% when discarding edges of the sample. On this first sample, $T_{max} = 330.2 \pm 1.3$ K, $\Delta P_m = 21.1 \pm 1.1$ $\mu\text{C cm}^{-2}$, $\Delta P_r = 3.4 \pm 0.2$ $\mu\text{C cm}^{-2}$ and $d_{33}^* = 42.3 \pm 2.9$ pm V^{-1} are obtained for the sample. All these elements reveal the capability of the deposition process to get homogeneous composition and dielectric/piezoelectric properties.

A sample with a composition gradient from BCTZ₅₀ to Ce_{0.2}:BCTZ₅₀ (0.2 mol%) has been elaborated. Even if the exact distribution of cerium is too small to be quantified using WDS, its presence is confirmed using XPS and its gradient is confirmed by the simultaneous evolution of the lattice parameter and the T_{max} which are largely affected. The quasi-continuous variation of the lattice parameter, representative of a quasi-continuous variation of the Ce content, allows evidencing a sharp peak in the piezoelectric coefficient in a very narrow doping window. The piezoelectric coefficient d_{33}^* increases by 50% from 42.3 ± 2.9 pm V^{-1} (undoped) to 63.0 ± 2.4 pm V^{-1} for 0.06% Ce-mol. This result reinforces the interest of the combinatorial approach and call for even finer phase diagrams exploration based on denser capacitors array, less steep nominal gradient and thorough x-ray micro-diffraction analysis.

Measurement as function of the AC field and Rayleigh analysis have been done to determine if change of piezoelectric properties may be induced by a higher extrinsic contributions (domain wall motion). For low cerium content, the domain wall motion contributions stay almost constant and then decrease when the cerium content increases. No correlation with the maximum of the d_{33}^* variation is observed, indicating that the increase of the piezoelectric coefficient is not induced by changes in dynamics and densities of domain walls. The measurements as a function of temperature reveal the energy landscape or the density of

domain wall in the film depends on the absolute temperature.

Supplementary Material

Supplementary material includes XRD and WDS characterizations.

Data availability

The data that support the findings of this study are available from the corresponding author upon reasonable request.

Acknowledgments

This work has been performed with the means of the CERTeM (microelectronics technological research and development center) of French region Centre Val de Loire. This work was funded through the project MAPS in the program ARD+ CERTeM 5.0 by the Région Centre Val de Loire co-funded by the European Union (ERC, DYNAMHEAT, N°101077402) and by the French State in the frame of the France 2030 program through the French Research Agency (ANR-22-PEXD-0018). Fruitful discussion with Jean-Louis Longuet from CEA-Le Ripault on WDS analysis are gladly acknowledged. Views and opinions expressed are however those of the authors only and do not necessarily reflect those of the European Union or the European Research Council. Neither the European Union nor the granting authority can be held responsible for them.

Conflict of Interest

The authors declare no competing financial interest.

References

- (1) Jayakrishnan, A.; Silva, J.; Kamakshi, K.; Dastan, D.; Annapureddy, V.; Pereira, M.; Sekhar, K. Are lead-free relaxor ferroelectric materials the most promising candidates for energy storage capacitors? *Progress in Materials Science* **2023**, *132*, 101046.
- (2) Veerapandiyan, V.; Benes, F.; Gindel, T.; Deluca, M. Strategies to Improve the Energy Storage Properties of Perovskite Lead-Free Relaxor Ferroelectrics: A Review. *Materials* **2020**, *13*, 5742.
- (3) Simon, Q.; Daumont, C. J. M.; Payan, S.; Gardes, P.; Poveda, P.; Wolfman, J.; Maglione, M. Extreme dielectric non-linearities at the convergence point in $\text{Ba}_{(1-x)}\text{Ca}_x\text{Ti}_{(1-y)}\text{Zr}_y\text{O}_3$ thin films. *Journal of Alloys and Compounds* **2018**, *747*, 366–373.
- (4) Daumont, C. J. M.; Simon, Q.; Le Mouellic, E.; Payan, S.; Gardes, P.; Poveda, P.; Negulescu, B.; Maglione, M.; Wolfman, J. Tunability, dielectric, and piezoelectric properties of $\text{Ba}_{(1-x)}\text{Ca}_x\text{Ti}_{(1-y)}\text{Zr}_y\text{O}_3$ ferroelectric thin films. *Journal of Applied Physics* **2016**, *119*, 094107, Publisher: American Institute of Physics.
- (5) Puli, V. S.; Pradhan, D. K.; Coondoo, I.; Panwar, N.; Adireddy, S.; Luo, S.; Katiyar, R. S.; Chrisey, D. B. Observation of large enhancement in energy-storage properties of lead-free polycrystalline $0.5(\text{Ba}_{0.7}\text{Ca}_{0.3}\text{TiO}_3) - 0.5(\text{BaZr}_{0.2}\text{Ti}_{0.8}\text{O}_3)$ ferroelectric thin films. *Journal of Physics D: Applied Physics* **2019**, *52*, 255304.
- (6) Yan, X.; Zheng, M.; Gao, X.; Zhu, M.; Hou, Y. High-performance lead-free ferroelectric BZT–BCT and its application in energy fields. *Journal of Materials Chemistry C* **2020**, *8*, 13530–13556.
- (7) Acosta, M.; Novak, N.; Rojas, V.; Patel, S.; Vaish, R.; Koruza, J.; Rossetti, G. A.; Rödel, J. BaTiO_3 -based piezoelectrics: Fundamentals, current status, and perspectives. *Applied Physics Reviews* **2017**, *4*, 041305.

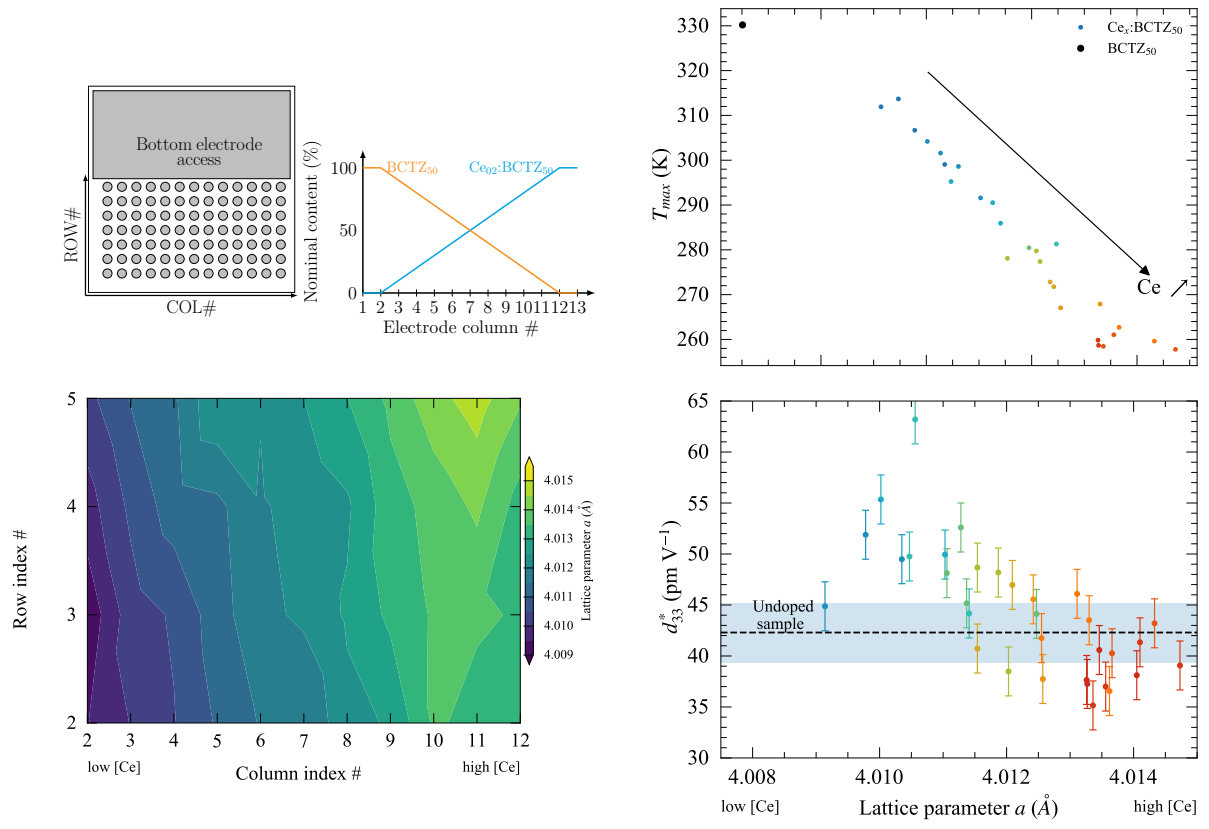
- (8) Zheng, M.; Zhao, C.; Yan, X.; Khachatryan, R.; Zhuo, F.; Hou, Y.; Koruza, J. Metal Particle Composite Hardening in $\text{Ba}_{0.85}\text{Ca}_{0.15}\text{Ti}_{0.90}\text{Zr}_{0.10}\text{O}_3$ Piezoceramics. *Advanced Functional Materials* **2023**, *33*, 2301356.
- (9) Carpenter, M. A. Static and dynamic strain coupling behaviour of ferroic and multiferroic perovskites from resonant ultrasound spectroscopy. *Journal of Physics: Condensed Matter* **2015**, *27*, 263201.
- (10) Damjanovic, D. Contributions to the Piezoelectric Effect in Ferroelectric Single Crystals and Ceramics. *Journal of the American Ceramic Society* **2005**, *88*, 2663–2676.
- (11) Ludwig, A. Discovery of new materials using combinatorial synthesis and high-throughput characterization of thin-film materials libraries combined with computational methods. *npj Computational Materials* **2019**, *5*.
- (12) Liu, G.; Wolfman, J.; Autret-Lambert, C.; Sakai, J.; Roger, S.; Gervais, M.; Gervais, F. Microstructural and dielectric properties of $\text{Ba}_{0.6}\text{Sr}_{0.4}\text{Ti}_{1-x}\text{Zr}_x\text{O}_3$ based combinatorial thin film capacitors library. *Journal of Applied Physics* **2010**, *108*, 114108.
- (13) Daumont, C.; Simon, Q.; Payan, S.; Gardes, P.; Poveda, P.; Maglione, M.; Negulescu, B.; Jaber, N.; Wolfman, J. Tunability Investigation in the BaTiO_3 - CaTiO_3 - BaZrO_3 Phase Diagram Using a Refined Combinatorial Thin Film Approach. *Coatings* **2021**, *11*, 1082.
- (14) Wolfman, J.; Negulescu, B.; Ruyter, A.; Niang, N.; Jaber, N. In *Practical Applications of Laser Ablation*; Yang, D., Ed.; IntechOpen: Rijeka, 2020; Chapter 1.
- (15) Hayati, R.; Bahrevar, M. A.; Ganjkhanelou, Y.; Rojas, V.; Koruza, J. Electromechanical properties of Ce-doped $(\text{Ba}_{0.85}\text{Ca}_{0.15})(\text{Zr}_{0.1}\text{Ti}_{0.9})\text{O}_3$ lead-free piezoceramics. *Journal of Advanced Ceramics* **2019**, *8*, 186–195.

- (16) Cui, Y.; Liu, X.; Jiang, M.; Zhao, X.; Shan, X.; Li, W.; Yuan, C.; Zhou, C. Lead-free $(\text{Ba}_{0.85}\text{Ca}_{0.15})(\text{Zr}_{0.1}\text{Ti}_{0.9})\text{O}_3\text{-CeO}_2$ ceramics with high piezoelectric coefficient obtained by low-temperature sintering. *Ceramics International* **2012**, *38*, 4761–4764.
- (17) Chandrakala, E.; Praveen, J. P.; Das, D. Effect of poling process on piezoelectric properties of BCZT – 0.08 wt.% CeO_2 lead-free ceramics. *AIP Conference Proceedings* **2016**, *1728*, 020502.
- (18) Ma, X. G.; Yan, C. L.; Li, Y. L.; Sang, R. L. Effect of different Ce_2O_3 on the structure and properties of BZT-CT ceramics. *Digest Journal of Nanomaterials and Biostructures* **2021**, *16*, 425–431.
- (19) Chandrakala, E.; John, P. P.; Palani, P.; Ganesan, M.; Das, D. Influence of Lattice Strain on Phase Transition and Piezoelectric Properties of Lead-Free $(\text{Ba}_{0.85}\text{Ca}_{0.15})(\text{Zr}_{0.1}\text{Ti}_{0.9})\text{O}_3$ Ceramics. *Transactions of the Indian Ceramic Society* **2020**, *79*, 144–151.
- (20) Nadaud, K.; Borderon, C.; Renoud, R.; Bah, M.; Ginestar, S.; Gundel, H. W. Dielectric, piezoelectric and electrostrictive properties of antiferroelectric lead-zirconate thin films. *Journal of Alloys and Compounds* **2022**, *914*, 165340.
- (21) Nadaud, K.; Borderon, C.; Renoud, R.; Bah, M.; Ginestar, S.; Gundel, H. W. Evidence of residual ferroelectric contribution in antiferroelectric lead-zirconate thin films by first-order reversal curves. *Applied Physics Letters* **2021**, *118*, 042902.
- (22) Nadaud, K.; Borderon, C.; Renoud, R.; Bah, M.; Ginestar, S.; Gundel, H. W. Metastable and field-induced ferroelectric response in antiferroelectric lead zirconate thin film studied by the hyperbolic law and third harmonic response. *Journal of Applied Physics* **2023**, *133*, 174102.
- (23) Nadaud, K.; Nataf, G. F.; Jaber, N.; Bah, M.; Negulescu, B.; Andreazza, P.; Birnal, P.; Wolfman, J. Subcoercive field dielectric response of

- 0.5 (Ba_{0.7}Ca_{0.3}TiO₃)–0.5 (BaZr_{0.2}Ti_{0.8}O₃) thin film: Peculiar third harmonic signature of phase transitions and residual ferroelectricity. *Applied Physics Letters* **2024**, *124*, 042901.
- (24) Ma, B.; Hu, Z.; Liu, S.; Tong, S.; Narayanan, M.; Koritala, R. E.; Balachandran, U. Temperature-dependent dielectric nonlinearity of relaxor ferroelectric Pb_{0.92}La_{0.08}Zr_{0.52}Ti_{0.48}O₃ thin films. *Applied Physics Letters* **2013**, *102*, 202901.
- (25) Liu, X.; Dai, Y.; Pei, X.; Chen, W. Giant room-temperature electrocaloric effect within wide temperature span in Sn-doped (Ba_{0.85}Ca_{0.15})(Zr_{0.1}Ti_{0.9})O₃ lead-free thin films. *Ceramics International* **2023**, *49*, 1846–1854.
- (26) Xu, X.; Yuan, G.; Xu, B.; Yin, J.; Liu, J.; Liu, Z. Influence of the Strain on Dielectric and Ferroelectric Properties of 0.5 (Ba_{0.7}Ca_{0.3}TiO₃)–0.5 (BaZr_{0.2}Ti_{0.8}O₃). *Journal of the American Ceramic Society* **2015**, *98*, 2823–2828.
- (27) Hwang, J. H.; Han, Y. H. Electrical Properties of Cerium-Doped BaTiO₃. *Journal of the American Ceramic Society* **2001**, *84*, 1750–1754, reprint: <https://onlinelibrary.wiley.com/doi/pdf/10.1111/j.1151-2916.2001.tb00910.x>.
- (28) Taylor, D. V.; Damjanovic, D. Evidence of domain wall contribution to the dielectric permittivity in PZT thin films at sub-switching fields. *Journal of Applied Physics* **1997**, *82*, 1973–1975.
- (29) Hall, D. A. Rayleigh behaviour and the threshold field in ferroelectric ceramics. *Ferroelectrics* *223*, 319–328.
- (30) Schenk, T.; Hoffmann, M.; Pešić, M.; Park, M. H.; Richter, C.; Schroeder, U.; Mikolajick, T. Physical Approach to Ferroelectric Impedance Spectroscopy: The Rayleigh Element. *Physical Review Applied* **2018**, *10*, 064004.

- (31) Taylor, D. V.; Damjanovic, D. Domain wall pinning contribution to the nonlinear dielectric permittivity in $\text{Pb}(\text{Zr}, \text{Ti})\text{O}_3$ thin films. *Applied Physics Letters* **73**, 2045–2047.
- (32) Borderon, C.; Renoud, R.; Ragheb, M.; Gundel, H. W. Description of the low field nonlinear dielectric properties of ferroelectric and multiferroic materials. *Applied Physics Letters* **2011**, *98*, 112903.
- (33) Bai, J.; Yang, J.; Zhang, Y.; Bai, W.; Lv, Z.; Tang, K.; Sun, J.; Meng, X.; Tang, X.; Chu, J. The ac sub-coercive-field dielectric resonances of $(\text{Pb}, \text{Sr})\text{TiO}_3$ films at low temperature. *Ceramics International* **2017**, *43*, S516–S519.
- (34) Boser, O. Statistical theory of hysteresis in ferroelectric materials. *Journal of Applied Physics* **1987**, *62*, 1344–1348.
- (35) Nadaud, K.; Sadl, M.; Bah, M.; Levassort, F.; Ursic, H. Effect of thermal annealing on dielectric and ferroelectric properties of aerosol-deposited $0.65 \text{Pb}(\text{Mg}_{1/3}\text{Nb}_{2/3})\text{O}_3 - 0.35 \text{PbTiO}_3$ thick films. *Applied Physics Letters* **2022**, *120*, 112902.
- (36) Borderon, C.; Brunier, A. E.; Nadaud, K.; Renoud, R.; Alexe, M.; Gundel, H. W. Domain wall motion in $\text{Pb}(\text{Zr}_{0.20}\text{Ti}_{0.80})\text{O}_3$ epitaxial thin films. *Scientific Reports* **2017**, *7*, 3444.
- (37) Bassiri-Gharb, N.; Fujii, I.; Hong, E.; Trolier-McKinstry, S.; Taylor, D. V.; Damjanovic, D. Domain wall contributions to the properties of piezoelectric thin films. *Journal of Electroceramics* **2007**, *19*, 49–67.
- (38) Garten, L. M.; Lam, P.; Harris, D.; Maria, J.-P.; Trolier-McKinstry, S. Residual ferroelectricity in barium strontium titanate thin film tunable dielectrics. *Journal of Applied Physics* **2014**, *116*, 044104.

- (39) Garten, L. M.; Burch, M.; Gupta, A. S.; Haislmaier, R.; Gopalan, V.; Dickey, E. C.; Trolier-McKinstry, S. Relaxor Ferroelectric Behavior in Barium Strontium Titanate. *Journal of the American Ceramic Society* **2016**, *99*, 1645–1650.
- (40) Everhardt, A. S.; Damerio, S.; Zorn, J. A.; Zhou, S.; Domingo, N.; Catalan, G.; Salje, E. K. H.; Chen, L.-Q.; Noheda, B. Periodicity-Doubling Cascades: Direct Observation in Ferroelastic Materials. *Physical Review Letters* **2019**, *123*.



For Table of Contents Only